Energy Advances

ROYAL SOCIETY OF CHEMISTRY

PAPER

View Article Online
View Journal | View Issue

Check for updates

Cite this: *Energy Adv.*, 2025, 4, 947

Renewable flower-based dye-sensitized solar cells using natural dye and natural carbon counter electrode†

Shunjian Xu,[a] Ping Huang,[*b] Wei Zhong,[b] Yongping Luo,[a] Haiyan Fu,[b] Zonghu Xiao,[b] Hong Jin[b] and Yike Liu*[a]

To advance the application of renewable biowaste in the renewable energy field, biowaste-derived natural dyes (BND) and biowaste-derived carbon materials (BCM) were individually prepared from five common flowers as raw materials and then facilely integrated into dye-sensitized solar cells (DSSCs). The five extracted BNDs contained anthocyanins with subtly different molecular structures, which were employed as photosensitizers to assemble mono-biowaste based devices with a Pt counter electrode, each of which showed a significantly different conversion efficiency (η), varying from 0.17% to 0.43%. The five pyrolyzed BCMs with an amorphous structure were used as counter electrodes to configure mono-biowaste based devices with the photosensitizer N719, and their η values ranged between 1.08% and 2.13%. The high efficiency of the BCM-based devices was mainly derived from their unique microstructure and the *N,S*-codoped oxygen-group-containing carbon skeleton of the BCM, which provided more catalytic active sites for reduction of the electrolyte. A dual-biowaste device based on crape myrtle violet flower with an η of 0.181% was finally fabricated by using the corresponding BND and BCM. Moreover, a combination strategy was carried out by introducing the BND extracted from willow leaf into the cell with the pyrolyzed crape myrtle violet flower BCM, resulting in an enhanced η of 0.32%.

Received 28th March 2025,
Accepted 27th May 2025

DOI: 10.1039/d5ya00086f

rsc.li/energy-advances

Open Access Article. Published on 31 May 2025. Downloaded on 5/31/2026 5:17:34 AM.
This article is licensed under a Creative Commons Attribution-NonCommercial 3.0 Unported Licence.

1. Introduction

In the low-carbon era, the utilization of renewable energy through devices made of renewable materials has become an inevitable development tendency.[1] As a cost-effective, colorful, and flexible photovoltaic device, dye-sensitized solar cells (DSSCs) consisting of a photosensitizer, photoanode, electrolyte and counter electrode, can convert solar energy into electrical energy for human consumption.[2–5] Two kinds of renewable materials in daily life, *i.e.*, biowaste-derived natural dyes (BND) and biowaste-derived carbon materials (BCM), can be facilely integrated into the DSSCs as the photosensitizer and counter electrode,[6–9] respectively. Utilizing both BND and BCM in the energy conversion field enables high-value-added use of renewable biowaste, which is otherwise commonly disposed through landfilling and incineration.

The photosensitizers in DSSCs play an indispensable role in absorbing sunlight and transforming photons to electrons.[6] Although the classical ruthenium complex dye (N719) used as the photosensitizer in these devices exhibits a remarkable conversion efficiency (η) of 12.3%, it has several disadvantages, such as the resource scarcity and high cost of the noble metal ruthenium.[10] To solve this problem, an alternative approach is the replacement of the N719 by BNDs, owing to their impressive features including abundance, easy preparation, and eco-friendly nature. BNDs have been extracted from natural leaves, stems, fruits, roots, hulls, flowers, *etc.*[11] In ancient China, BNDs with coloring compositions were broadly applied in dying textiles.[12] At present, BNDs in the form of carotenoids, flavonoids, chlorophylls, and anthocyanins have been introduced as the photosensitizer in the DSSCs.[13]

The counter electrode in DSSCs serves to collect the external electrons and to reduce the electrolyte.[14] The noble metal Pt is a typical electrode catalyst due to its high catalytic activity. Nevertheless, the high cost, resource scarcity, and poor stability of Pt films in corrosive electrolytes (leading to the formation of PtI_4) limit its widespread application.[15,16] Accordingly, renewable BCMs have attracted attention as electrode catalysts to replace Pt, due to their relatively low cost, excellent chemical stability,

[a] *Xisai Mountain New Energy Research Institute, School of Intelligent Manufacturing, Huzhou College, Huzhou 313000, China. E-mail: liuyike@zjhzu.edu.cn*
[b] *School of New Energy Science and Engineering, Xinyu University, Xinyu 338004, China. E-mail: Ph0603@163.com*

† Electronic supplementary information (ESI) available. See DOI: https://doi.org/10.1039/d5ya00086f

© 2025 The Author(s). Published by the Royal Society of Chemistry

Open Access Article. Published on 31 May 2025. Downloaded on 5/31/2026 5:17:34 AM. This article is licensed under a Creative Commons Attribution-NonCommercial 3.0 Unported Licence.

and reasonable catalytic properties.[8,17,18] In particular, using BCMs avoids the complex synthesis processes associated with other carbon materials, such as carbon nanotubes,[19] carbon black,[20] and graphene.[21] BCMs have been fabricated using the same biowastes employed for BND extraction through simple high-temperature pyrolysis.[22,23] The obtained BCMs have been applied in many technological fields other than DSSCs, for example, water purification,[24] gas adsorption,[25] supercapacitors,[26] and lithium/sodium ion batteries.[27,28] To date, limited work to realize the full potential of pyrolyzed flower BCMs in DSSCs has been performed. At the same time, previous research into wood- and leaf-derived BCMs has revealed that the η of BCM-derived DSSCs is highly dependent on the morphology and microstructure of the BCM, which mainly originate from the biowaste selected.[17,18,29,30] In particular, to our knowledge, a few reports have paid close attention to the integration of a renewable BND and BCM in the same device to replace the N719 photosensitizer and Pt catalyst, respectively.

Colorful and diverse flowers adorn a beautiful world. Unfortunately, they instantly become biowaste after withering. In this research, to advance the application of renewable biowaste in the renewable energy field, BNDs and BCMs were first individually prepared using five common flowers as raw materials *via* the facile techniques of ethanol extraction and one-step pyrolysis, respectively and were then employed to assemble renewable-flower-based DSSCs with mono-biowaste-based and dual-biowaste-based modes. In the dual-biowaste-based mode, the BND and BCM were employed as the photosensitizer and counter electrode catalyst, respectively, as shown in Fig. 1. The flowers employed were lotus, oleander, crape myrtle violet, crape myrtle white, and hibiscus. Some of these flowers, such as the two crape myrtle varieties, were introduced into DSSCs for the first time in this study. Furthermore, we focused on a combination strategy for strengthening the photovoltaic properties of the dual-biowaste-based DSSCs by introducing a willow-leaf-extracted BND into a cell with the pyrolyzed crape myrtle violet flower BCM, resulting in an enhanced η of 0.32%.

In terms of the scientific novelty or advancement in this study, there are several aspects: (1) Although several of the flowers used have already been reported in the literature as sensitizers, crape myrtle violet flower and crape myrtle white flower are employed here for the first time to prepare natural dyes for DSSCs. Furthermore, the solid residues of these five flowers were simultaneously pyrolyzed to fabricate carbon materials as counter electrodes for DSSCs, which has never been reported before. (2) Despite the low photovoltaic efficiencies of these biomass-based DSSCs, we designed several improvement strategies to achieve better performance. For the dual-biowaste-based mode, a biomass with good light absorption performance may not necessarily have good catalytic performance. Hence, we conducted cross-combination studies of different BNDs and BCMs. In addition, we explored the co-sensitization strategy to compensate for the weak light absorption ability of a single natural dye. (3) The study on the morphological and structural characteristics of renewable pyrolyzed flower BCMs has yielded some interesting findings, which can provide a reference for the current research into negative electrode materials for sodium ion batteries. For example, the flakes with nanopores and amorphous structure of the BCM could be partially split up into independent nanobelts after milling.

2. Experimental details

2.1. Fabrication of BNDs and BCMs

Five species of fresh flowers were collected from the corresponding plants in the central part of China. The petals were detached from the flowers and used as the raw materials to synthesize the BNDs and BCMs. The petals were first washed to remove pollutants, dried at room temperature, and then heated at 80 °C. The dried petals were milled to obtain the petal powders for the BND extraction and BCM pyrolysis.

10 g of the petal powder was immersed in 100 mL ethanol for 12 h at room temperature. The mixed solution was filtered using filter paper to remove solid residue, producing the BND extract solution. The extracted BND solution was stored at 4 °C and used for the sensitization of the TiO_2 photoanode. The filtered solid residue was further pyrolyzed at 800 °C for 1 h in an N_2 atmosphere to form the BCM. The obtained BCM was finally milled to give BCM powder for preparing the BCM counter electrode. For brevity, the BNDs extracted from the lotus flower, oleander flower, crape myrtle violet flower, crape myrtle white flower, and hibiscus flower are referred to as the BND-LF, BND-OF, BND-VF, BND-WF, and BND-HF, respectively, while the BCMs pyrolyzed from those flowers are respectively designated as BCM-LF, BCM-OF, BCM-VF, BCM-WF, and BCM-HF.

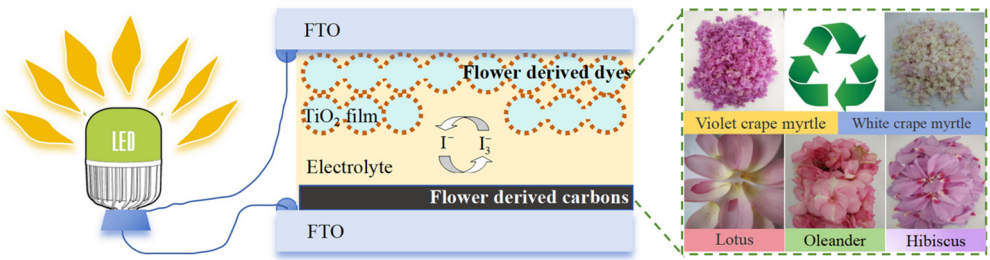

Fig. 1 Schematic of DSSCs consisting of natural anthocyanin dyes and natural carbon counter electrodes derived from renewable flowers.

© 2025 The Author(s). Published by the Royal Society of Chemistry

Open Access Article. Published on 31 May 2025. Downloaded on 5/31/2026 5:17:34 AM. This article is licensed under a Creative Commons Attribution-NonCommercial 3.0 Unported Licence.

2.2. Configuration of devices

The DSSCs with a typical sandwich structure were configured by stacking a BND-sensitized TiO_2 photoanode, an LiI/I_2 electrolyte and a BCM counter electrode. Although ITO has better conductivity, FTO has better high-temperature resistance and corrosion resistance, as well as lower cost. During the preparation of the photoanode and counter electrode of the DSCCs, high-temperature sintering is required. Although AZO inexpensive, its performance is inferior than those of ITO and FTO. Considering the above, FTO was chosen for this study. The BND-sensitized TiO_2 photoanode was prepared by immersing the TiO_2 photoanode composed of mesoporous TiO_2 film and FTO into the BND solution at room temperature for 24 h. The dye loading amount is important for light absorption and device performance. However, excessive adsorption of dyes may clog the TiO_2 pores, hinder the penetration of the electrolyte and the transfer of charge and thus reduce the efficiency of the DSSCs. The adsorption of a monolayer on the surface of TiO_2 can ensure sufficient light absorption while avoiding the adverse effects mentioned above, as shown in Fig. 1. Thus, we removed the excess dye from the BND-sensitized TiO_2 photoanodes with alcohol. BCM electrodes with a carbon loading of about 3 mg cm^{-2} were prepared by coating a blended BCM paste on FTO, followed by annealing in air at 120 °C for 2 h. To obtain the blended paste, the BCM was ground in a mortar with carboxymethyl cellulose (CMC) and aqueous alcohol. The fabrication process of the TiO_2 photoanode and the LiI/I_2 electrolyte was previously described.[17,18]

2.3. Characterizations and measurements

The ultraviolet-visible light (UV-Vis) spectra and Fourier transform infrared (FT–IR) spectra of the BND solutions were obtained using a double-beam UV-Vis spectrophotometer (TU-1901, Persee, China) and an FT–IR spectrometer (Nicolet5700, Thermo, USA), respectively. The FT-Raman spectra of the BND solutions were measured using a FT-Raman spectrometer (Nicolet IS50, Thermo, USA). The morphologies and microstructures of the BCMs were observed using scanning electron microscopy (SEM; EVO MA10, Zeiss, Germany) and high-resolution transmission electronic microscopy (TEM; JEM-2100, JEOL, Japan). The crystal structures of the BCMs were characterized using X-ray diffraction (XRD; D8 ADVANCE, Bruker, Germany) with Cu Kα radiation. The N_2 adsorption–desorption isotherms of the BCMs were recorded using an automatic adsorption instrument (ASAP 2020M, Micromeritics, USA), under nitrogen at 77 K. The surface areas (S_{BET}) and pore size distributions of the BCMs were calculated using the Brunauer–Emmett–Teller (BET) and Barrett–Joyner–Halenda (BJH) methods, respectively. X-ray photoelectron spectroscopy (XPS) of the BCMs was performed using a spectrometer (K-alpha, ThermoFisher, UK) with monochromatic Al Kα radiation. Thermogravimetric analysis (TGA) and differential thermal analysis (DTA) of the dried petals were recorded using a thermogravimeter (STA2500, NETZSCH, Germany). These samples were heated to 1000 °C at a rate of 10 °C min^{-1} in N_2. Measurements of the Nyquist plots and Tafel polarization curves were conducted with an electrochemical workstation based on a symmetric cell consisting of two identical counter electrodes and an electrolyte. The photocurrent–voltage (J–V) performances of the devices were measured under illumination with a standard light intensity.

3. Results and discussion

3.1. Photovoltaic properties of renewable-flower-based DSSCs

The flower-extracted BNDs were first used as the photosensitizer to assemble the mono-biowaste-based DSSCs with a Pt counter electrode, and their J–V curves and photovoltaic parameters are illustrated in Fig. 2(a). The significant differences in the η and short-circuit photocurrent density (J_{sc}), both of which have similar tendencies, are observed in the five BND-based devices. According to the values of both parameters for the devices, the five BNDs could be divided into three grades in the sequence grade I > grade II > grade III. The oleander-flower-derived extract was of grade I, that is, its device exhibited the highest values of η (0.43%) and J_{sc} (1.29 mA cm^{-2}) among the five BND-based devices. Grade II includes the two crape myrtle flower extracts, which demonstrated almost same values of η and J_{sc}, while the grade III comprises the lotus and hibiscus flower extracts. The η values of BND-VF, BND-WF, BND-HF, and BND-LF are 0.30%, 0.30%, 0.18%, and 0.17%, respectively. Moreover, the variation in the open-circuit voltage (V_{OC}) and fill factor (FF) of the five BND-based devices was relatively small, with ranging 0.485–0.511 V and 0.59–0.65, respectively, as displayed in Fig. S1 (ESI†). The above results indicate that the enhanced J_{sc} is a dominant contribution to strengthening the η of the BND-based device.

The pyrolyzed flower BCMs were then used as catalytic films to assemble the mono-biowaste-based DSSCs with N719 photosensitizer, and their J–V curves and photovoltaic parameters are presented in Fig. 2(b) and Fig. S1 (ESI†). The η values of the BCMs derived from the five flowers used in the devices followed the sequence crape myrtle violet flower > crape myrtle white flower > lotus flower > oleander flower > hibiscus flower, which differs significantly from the trend observed in devices employing the corresponding flower-derived BNDs. The values of η are 2.13%, 1.91%, 1.56%, 1.21%, and 1.08% for BCM-VF, BCM-WF, BCM-LF, BCM-OF and BCM-HF, respectively. The high efficiency of the BCM-based devices is mainly due to the large FF. To reveal the differences in their photovoltaic performances, three representative BCMs, namely, BCM-VF, BCM-WF, and BCM-HF, were further selected to understand their comparative electrochemical performances. The charge-transfer resistance (R_{ct}) and exchange current density (J_0) were obtained from the Nyquist plots and Tafel polarization curves, respectively, as displayed in Fig. 3. Specifically, the R_{ct} is determined from the diameter of semicircle at high-frequency in the Nyquist plot, while the J_0 corresponds to the intersection of the tangent line of the Tafel zone and the extension line of the zero bias. Obviously, BCM-VF and BCM-WF exhibited smaller R_{ct} and larger J_0 values than BCM-HF. This indicates

Open Access Article. Published on 31 May 2025. Downloaded on 5/31/2026 5:17:34 AM. This article is licensed under a Creative Commons Attribution-NonCommercial 3.0 Unported Licence.

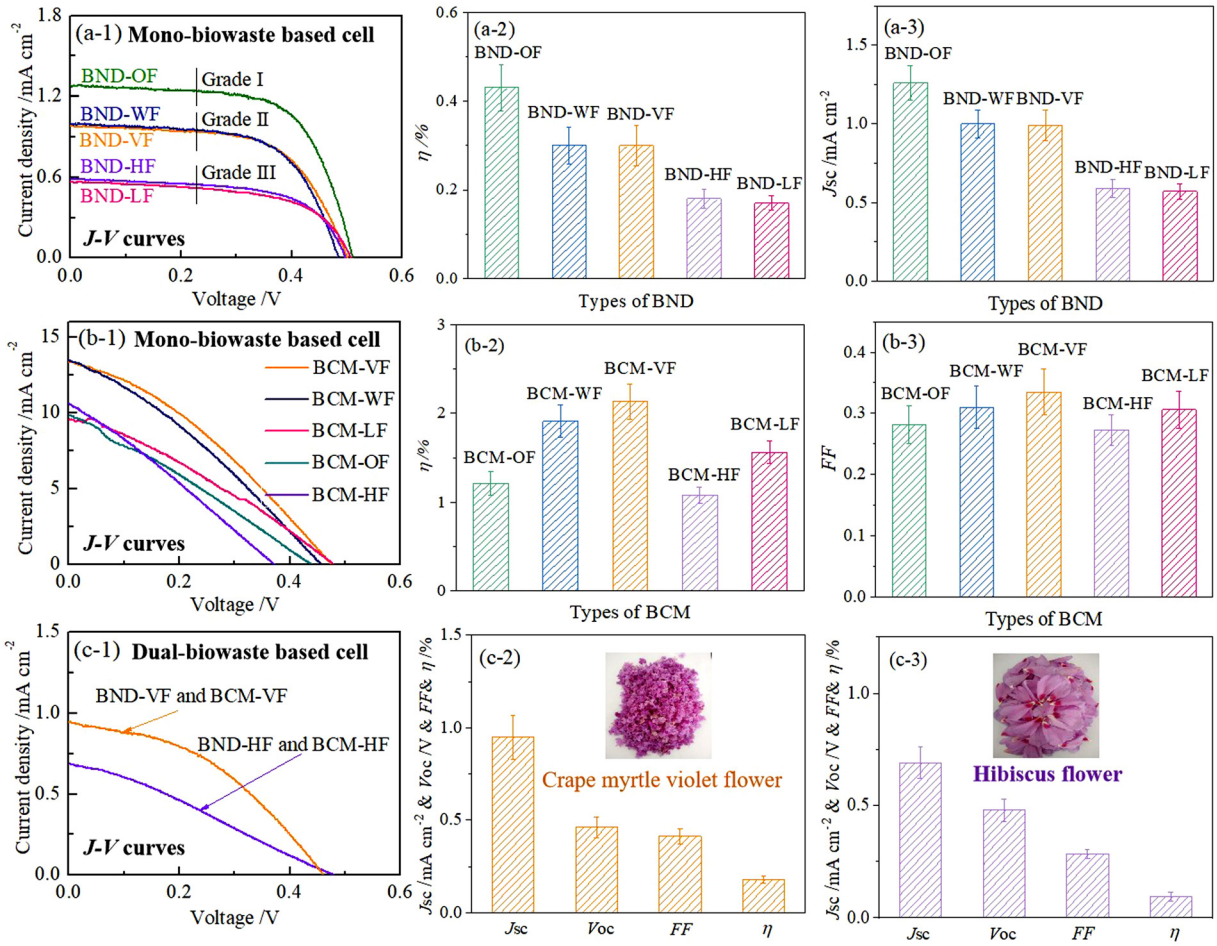

Fig. 2 *J–V* curves and photovoltaic parameters of renewable-flower-based DSSCs with various modes. (a) Mono-biowaste-based cells using a BND dye and Pt electrode; (b) mono-biowaste-based cells using N719 dye and a BCM electrode; (c) dual-biowaste-based cells using a BND dye and BCM electrode.

that both the crape-myrtle-flower-derived BCMs have superior catalytic activity for the reduction of tri-iodide (I_3^-) compared to the hibiscus-flower-derived BCM, which is a key factor to endow the devices with more outstanding photovoltaic performances. Furthermore, the analogous electrochemical parameters of BCM-VF and BCM-WF imply that both pyrolyzed crape myrtle flower BCMs exhibit similar catalytic activity, resulting in the similar photovoltaic properties for the cells.

As the crape myrtle violet flower provides both a pronounced dye and the most excellent catalyst among the five flowers for the devices, dual-biowaste-based DSSCs were fabricated using BND-VF as the photosensitizer and BCM-VF as the electrode catalyst. The corresponding *J–V* curve and photovoltaic performance are shown in Fig. 2(c). Compared with the mono-biowaste-based mode device, the η of the dual-biowaste-based mode device obviously declines to 0.181%. However, the η of the crape-myrtle-violet-flower-based device is far superior to that of the hibiscus-flower-based one; the η value of the latter cell is only 0.094%. The *J–V* curves of DSSCs using N719 and Pt are shown in Fig. S2 in ESI,† and the η of the DSSCs reached as high as 6.44%. The results indicate that the development of fully biomass-based DSSCs remains in its early stages and requires further advancement.

3.2. Spectral and structural characteristics of BNDs extracted from renewable flowers

The UV-Vis technique provides necessary information on the solar energy range absorbed by a dye. The obtained UV-Vis absorption spectra of the BND solutions are demonstrated in Fig. 4(a). All the BNDs are light yellow and soluble in ethanol, and they exhibit a similar absorption range of visible light wavelengths, mainly concentrated from 300 to 400 nm. According to the intensities and positions of the absorption peaks, the five absorption curves could be classified into three styles, which corresponded with the η and J_{sc} values of the mono-biowaste-based devices employing the natural dyes (Fig. 2a). The oleander-flower-extracted BND-OF is of style I, while crape-myrtle-flower-extracted BND-VF and BND-WF are both of style II. Compared to the style II curves, the absorption peak of the style I curve exhibits an ultraviolet shift and presents at 326 nm. However, the absorption intensity of the style I curve in the range from 350 to 400 nm approaches that of style II. Style III

© 2025 The Author(s). Published by the Royal Society of Chemistry

Open Access Article. Published on 31 May 2025. Downloaded on 5/31/2026 5:17:34 AM. This article is licensed under a Creative Commons Attribution-NonCommercial 3.0 Unported Licence.

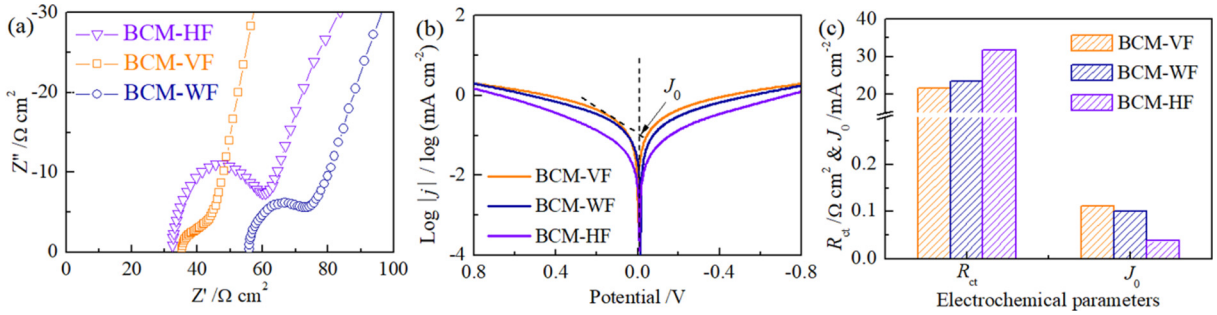

Fig. 3 Electrochemical performances of the various BCM counter electrodes. (a) Nyquist plots; (b) Tafel polarization curves; (c) electrochemical parameters extracted from (a) and (b).

includes BND-LF and BND-HF, which were extracted from lotus and hibiscus flowers, respectively. The absorption intensity of the style III curves is evidently lower than that of the other two styles. Moreover, the conclusions reflected by the absorption spectra are in good agreement with the transmission spectra results shown in Fig. 4(b). Evidently, the strengthened photon capture capability of the BND is a determining factor in inducing the high η and J_{sc} of the BND-based devices. As shown in Fig. 2(a), the BCM-OF based DSSC exhibited the highest η (0.43%). Therefore, taking BCM-OF as an example, we measured the UV-Vis diffuse reflectance absorption spectrum of the dye-adsorbed TiO_2 photoanode. As shown in Fig. S3 (ESI†), the absorption range of the dye-absorbed TiO_2 photoanode was mainly concentrated in the ultraviolet band, which made the efficiency of the DSSCs much lower than that of commercial dyes like N719.

The FT-IR technique was further employed to characterize the flower-extracted BNDs. Fig. 4(c) presents the FT-IR spectra of three BND solutions that represent the three styles of the absorption spectra in Fig. 4(a). It is clear that the three natural dyes display similar spectral profiles with different intensities, indicating homologous main active ingredients in all the BNDs. In the spectra of all the BNDs, the bands appearing at 1330–1381 cm^{-1} are assigned to the C–O angular deformations of phenols, while the bands at 1454–1651 cm^{-1} correspond to the C=C stretching vibration of aromatic rings.[31] Note that the intensities of the above peaks for BND-OF (style I) are obviously stronger than those of the corresponding peaks for both BND-VF (style II) and BND-HF (style III). In particular, the peak observed at 1454 cm^{-1} for both BND-OF and BND-VF is shifted to 1435 cm^{-1} for BND-HF. This suggests that the main active ingredients in BND-OF and BND-VF have a more integrated molecular structure compared to those in BND-HF, thereby enhancing photon capture in the devices. Furthermore, the peak at 1416 cm^{-1} is attributed to the νC=N hydroxyl (–OH) or –NH group. The two peaks near 2975 cm^{-1} and 2894 cm^{-1} are assigned to the symmetric stretching modes of CH, whereas the broadest peak at 3376 cm^{-1} was assigned to the O–H stretching vibration of the BND solutions, including water and ethanol.[32] Obviously, the FT-IR results confirm the existence of anthocyanins

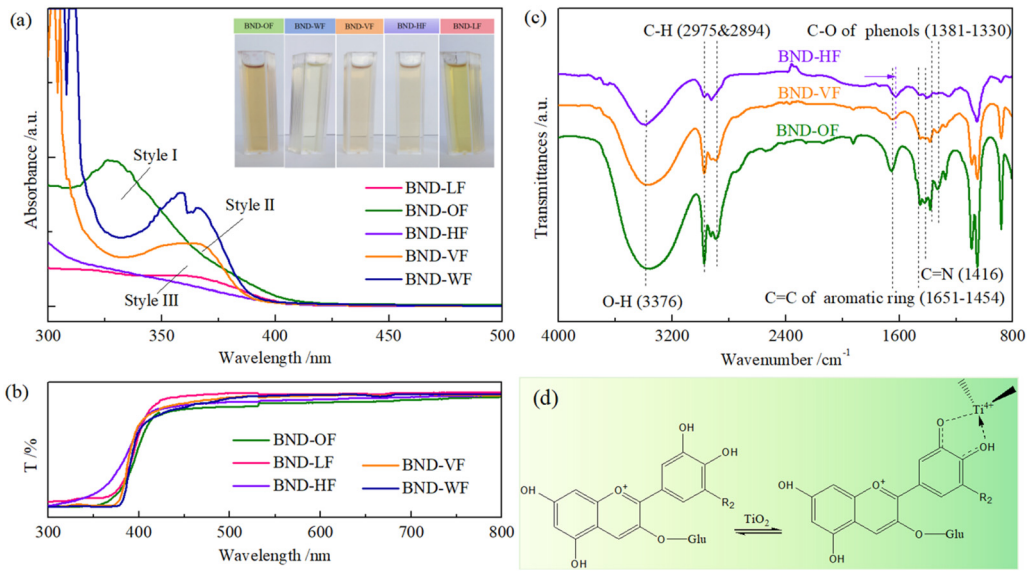

Fig. 4 Spectral and structural characteristics of various flower-extracted BND solutions. (a) UV-Vis absorption spectra; (b) UV-Vis transmission spectra; (c) FT-IR spectra; (d) chemical structure of anthocyanin in the BND and its bonding interaction with TiO_2. The insert in (a) shows photos of the BND solution.

Open Access Article. Published on 31 May 2025. Downloaded on 5/31/2026 5:17:34 AM.
This article is licensed under a Creative Commons Attribution-NonCommercial 3.0 Unported Licence.

with subtle structural differences as the main active ingredient in all the flower-derived BNDs. The anthocyanin consists of an aglycone or anthocyanidin moiety flanked with sugars and acyl groups.[33] This belongs to the flavonoid family with a flavylium cation as the core unit. The anthocyanin can be anchored on the TiO_2 surface by substitution of the surface hydroxyl moieties with Ti(IV) from the TiO_2 photoanode, creating an electron transfer route.[7] The chemical structure of the anthocyanin and its bonding interaction with the TiO_2 are shown in Fig. 4(d). The Raman spectra in Fig. S4 (ESI†) were obtained to confirm the presence of anthocyanins as the main active ingredients in the BNDs. The peak at 1620 cm^{-1} is attributed to the C=C stretching vibration of the benzene ring, while the peaks in the range of 1050–1150 cm^{-1} are ascribed to the stretching vibration of the glycosidic bond (C–O–C). The peak at 1276 cm^{-1} is assigned to the stretching vibration of C–O on the benzene ring or the bending vibration within the C–H plane, while the peak at 1453 cm^{-1} is assigned to the C–H bending vibration or C–C stretching vibration of the benzene ring. The peaks around 1300 cm^{-1} are related to the vibrations of the –OH.

As revealed in Table S1 (ESI†), we tested other natural dyes, including various leaves, petals, and peels, but the PCEs obtained for the DSSCs were also much lower than those of commercial dyes. Possible reasons include: (1) the narrow absorption spectrum range of natural dyes, (2) poor energy level matching between natural dyes and semiconductors, (3) easy photodegradation or chemical decomposition of natural dyes in electrolyte, and (4) non-conjugated groups of natural dyes reducing charge separation efficiency. In addition, the natural dyes obtained from the current experiment contain other impurities. If further purification were carried out, the PCE could be improved.

3.3. Morphological and structural characteristics of renewable pyrolyzed flower BCMs

To explore the origin of the electrochemical performance of the three representative BCMs, that is, BCM-VF, BCM-WF, and BCM-HF, their morphological and structural features were comparatively analyzed. The SEM images in Fig. 5(a)–(f) show that the BCM-VF and BCM-WF derived from the two crape myrtle flowers possess almost identical surfaces and fractures, which are different to those of the BCM-HF prepared from the hibiscus flower. A large number of mountain-chain-like flakes with a thickness of less than 1 μm are regularly arrayed on both the BCM-VF and BCM-WF. The fine flakes have nano-scale wrinkle-like microstructures, which resemble "terraced fields" on the mountains. After milling the BCM, the flakes with nanopores and amorphous structure could be partially split

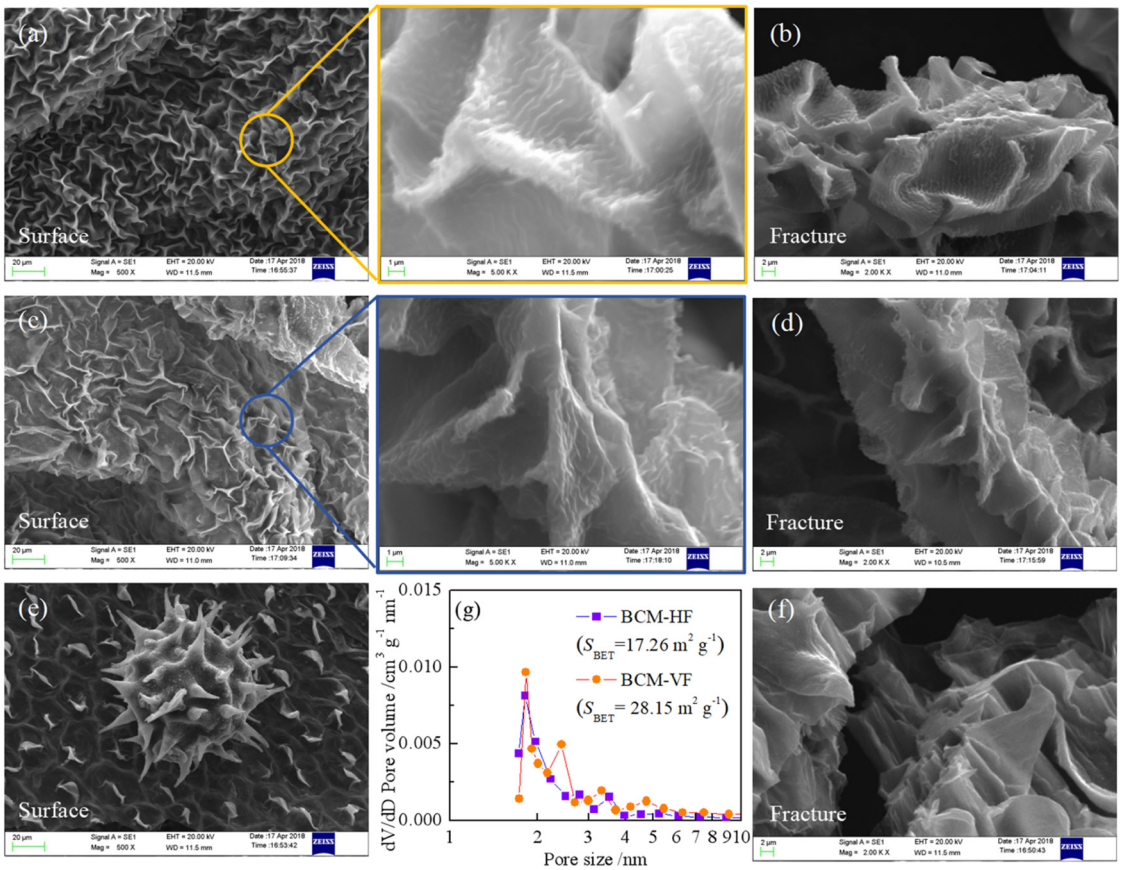

Fig. 5 Morphological and porous characteristics of various pyrolyzed flower BCMs. (a) and (b) SEM images of BCM-VF; (c) and (d) SEM images of BCM-WF; (e) and (f) SEM images of BCM-HF; (g) pore size distributions of BCM-VF and BCM-HF.

© 2025 The Author(s). Published by the Royal Society of Chemistry

Open Access Article. Published on 31 May 2025. Downloaded on 5/31/2026 5:17:34 AM. This article is licensed under a Creative Commons Attribution-NonCommercial 3.0 Unported Licence.

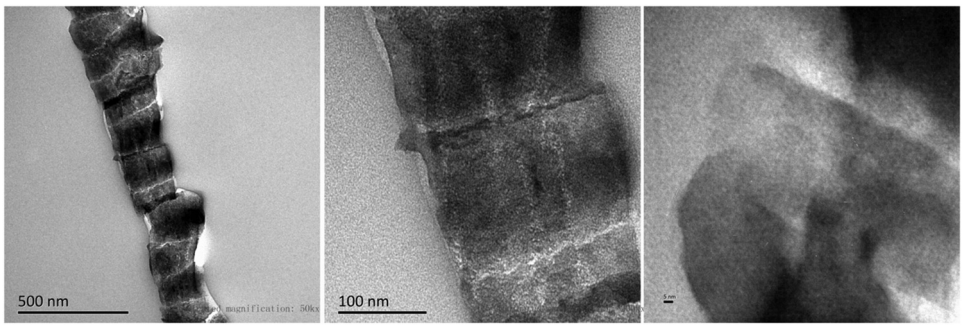

Fig. 6 TEM morphology of BCM-VF derived from crape myrtle violet flower.

up into independent nanobelts, as illustrated in the TEM images (Fig. 6). In comparison, the unique wrinkle-like microstructures are nearly absent on the homologous flakes with less quantity for BCM-HF. This implies that both BCM-VF and BCM-WF possess higher surface area than the BCM-HF. In addition, the pore size distributions of the BCM in Fig. 5(g) further reveal that the volume of the pores in the BCM-VF, which range from 2 to 3 nm, is greater than that of those of BCM-HF, which also brings about the larger surface area for the former BCM. The values of S_{BET} are 28.15 and 17.26 $m^2\ g^{-1}$ for BCM-VF and BCM-HF, respectively. Thus, the pyrolyzed BCM derived from crape myrtle flowers, with its unique microstructure and larger surface area, can offer more catalytically active sites for I_3^- reduction than the BCM prepared from hibiscus flowers. This is a key factor contributing to the enhanced catalytic performance of the natural carbon materials.

The XRD patterns of the three representative BCMs are shown in Fig. 7(a). It is obvious that all the carbon materials have almost the same diffraction patterns, indicating their extremely similar crystal structures. The existence of two broadening diffraction peaks of (002) and (100) associated with graphite characteristics implies that the skeletons of all the BCM are of the glassy carbon type, which is a general structural feature of the carbon materials derived from the cellulose-based biowastes, such as leaves, paper and wood.[18,34] Glassy carbon consists of abundant and randomly oriented graphene stacks, and the catalytic active sites are located at the edges of the graphene stacks.[35] Therefore, all the BCMs can contribute to I_3^- reduction in the counter electrode. Furthermore, several tiny but clearly identifiable diffraction peaks can be also seen in all the XRD patterns, indicating the presence of a few impurities in the carbon skeletons of all the BCMs. These diffraction peaks mainly correspond to five minerals, including calcite ($CaCO_3$), sylvite (KCl), wollastonite ($CaSiO_3$), butschliite ($K_2Ca(CO_3)_2$) and quicklime (CaO).[36,37]

XPS was further used to extract the surface information of BCM-VF derived from the crape myrtle violet flower. The XPS survey spectrum in Fig. 7(b) shows that BCM-VF is mainly composed of carbon and oxygen with an O 1s/C 1s atomic ratio of 0.323. The high-resolution C 1s spectrum of BCM-VF in Fig. 7(c) reveals a peak at 284.4 eV, which is attributed to graphite-like carbon with a relative content of 84.48%, which is consistent with the XRD and TEM analyses (Fig. 6 and 7a). The remaining two peaks at 285.2 and 287.2 eV are related to the ether/alcohol and the carbonyl (C═O), respectively.[26] The presence of the oxygen-containing groups is confirmed by the O 1s spectrum in Fig. 7(d). The peaks at 531.1, 532.1, and 533.2 eV are respectively ascribed to the carbonyl (C═O), the hydroxyl (–OH) and non-carbonyl oxygen (ether structure) in the ester, and the carboxyl (–COOH), with relative contents of 13.62%, 54.23%, and 32.15%. These oxygen-containing groups at the sharp atomic edges in the BCM can act as the catalytic active sites. More information can be obtained from Fig. 7(b), which shows that four weak peaks occur at around 169, 233, 293, and 401 eV, which are attributed to S 2p, Si 2p, K 2p, and N 1s, respectively. Among them, the amounts of sulfur and nitrogen are 5.36% and 1.35%, respectively. The moderate amounts of nitrogen and sulphur present in the BCM-VF enhance its catalytic activity, owing to the high charge polarisation and the asymmetric distribution of the atomic charge density in the C atoms,[38,39] respectively. Through fitting analysis, the sulfur peaks were determined to be related to –C–SO_3– and –C–SO_4– bonds (Fig. 7e), while the nitrogen peak is attributed to hexagonal pyridinic-N and the quaternary nitrogen bound within a graphitic-like framework (Fig. 7f).[40] Furthermore, the trace silicon and potassium observed indirectly indicates that K- and Si-containing minerals were present in the BND-VF.

The formation of the amorphous carbon in BCM-VF from the dried crape myrtle violet flower was explored using the TGA and DTA techniques. As displayed in Fig. 7(g), the weight loss behavior of the flower can be divided into four distinguished stages with increasing temperature. In stage I (25–150 °C), the mass loss of the sample with a remaining weight of 95.38 at 150 °C is mainly due to the moisture removal in the flower. In the stage II (150–390 °C), the mass loss of the sample with a remaining weight of 63.03% at 390 °C is mainly attributed to the breakage of the hemicellulose and cellulose in the flower.[17] Meanwhile, the first exothermic peak occurs at around 320 °C. In stage III (390–700 °C), the mass loss of the sample with a remaining weight of 32.27% at 700 °C is caused by the degradation of the lignin in the flower. At the same time, the second and third exothermic peaks arise at about 453 and 516 °C, respectively. Above 700 °C, stage IV of the formation and graphitization of the glassy carbon in the BCM takes place,

Open Access Article. Published on 31 May 2025. Downloaded on 5/31/2026 5:17:34 AM.
This article is licensed under a Creative Commons Attribution-NonCommercial 3.0 Unported Licence.

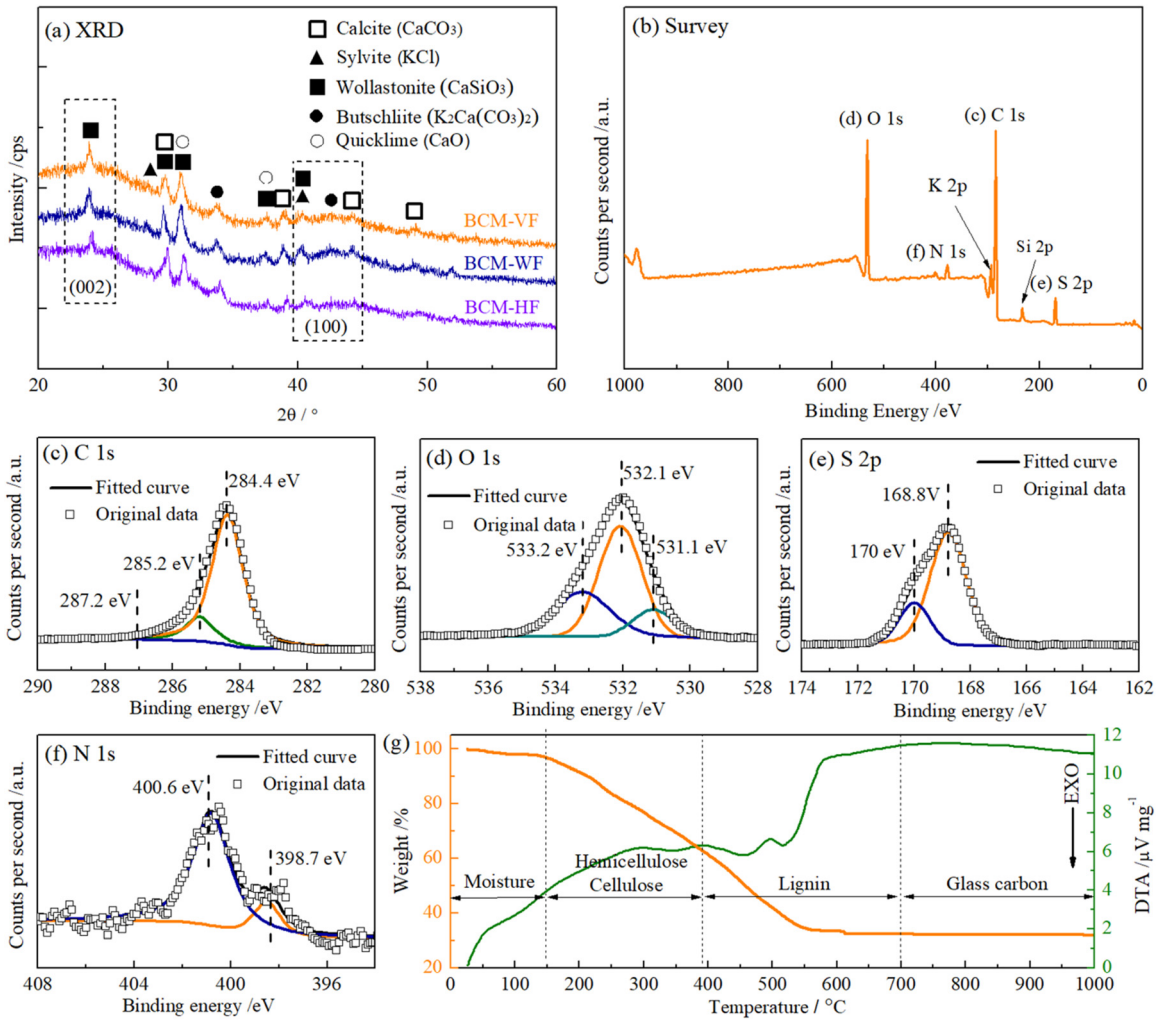

Fig. 7 Structure and surface characteristics of various pyrolyzed flower BCMs. (a) XRD patterns. (b) XPS survey spectrum and high-resolution scans of the (c) C 1s, (d) O 1s, (e) S 2p and (f) N 1s regions of BCM-VF. (g) TGA and DTA curves of the dried crape myrtle violet flower used for BCM-VF preparation.

and 32.16% of the sample is left at the end of TGA experiment conducted at 1000 °C. The final residues are mainly composed of dual-doped amorphous carbon with minor mineral substances and chemical groups.

3.4. Combination strategy to strengthen dual-biowaste-based DSSCs

To further enhance the η of the dual-biowaste-based DSSCs derived from crape myrtle violet flowers, a potential approach is to replace the BND-VF with another BND that exhibits stronger photon-capturing ability. Previous research, including research by our group, has revealed that BNDs extracted from leaves containing chlorophyll acted as a main active ingredient.[9,11,13,17] The chlorophyll could be bonded to the surface of TiO_2 *via* $C^{x}{=}O\cdots TiO_2$ coordination. Note that the absorption range of the leaf-derived BND in visible-light is generally wider than that of the flower-derived ones, indicating a stronger photon-capturing ability of the former BND. Considering the potential advantages of the leaf-extracted BNDs, the willow leaves were used for the first time as a new raw material for BND extraction using the same process, and the resulting dye is denoted as BND-WL. The UV-Vis and FT-Raman spectra in Fig. 8(a) and (b) confirm that the BND-WL also possesses chlorophyll. Using the formula $E = hc/\lambda$, band gaps of 1.87 eV and 3.42–3.79 eV were calculated for the BNDs derived from willow leaf and the five flowers, respectively, where h is Planck's constant, λ is the wavelength of the absorption spectrum peak, and c is the speed of light.[9] A narrow band gap indicates strong photon-capturing ability of BND. When BND-WL was used in the mono-biowaste-based DSSCs with a Pt electrode, a higher η of 0.627% was obtained in comparison with all the flower-extract BNDs, as shown in Fig. 8(c) and (d). However, the pyrolyzed willow leaf BCM exhibits weak catalytic activity, resulting in a low η (1.26%) when used in the mono-biowaste-based device with N719 dye. Therefore, only the willow-leaf-extracted BND-WL was employed as a photosensitizer to assemble dual-biowaste-based DSSCs with the crape myrtle violet flower pyrolyzed BCM-VF electrode. The η of this device increased to 0.32%, which is 76.24% higher than that of the device with BND-VF dye

© 2025 The Author(s). Published by the Royal Society of Chemistry

Open Access Article. Published on 31 May 2025. Downloaded on 5/31/2026 5:17:34 AM.
This article is licensed under a Creative Commons Attribution-NonCommercial 3.0 Unported Licence.

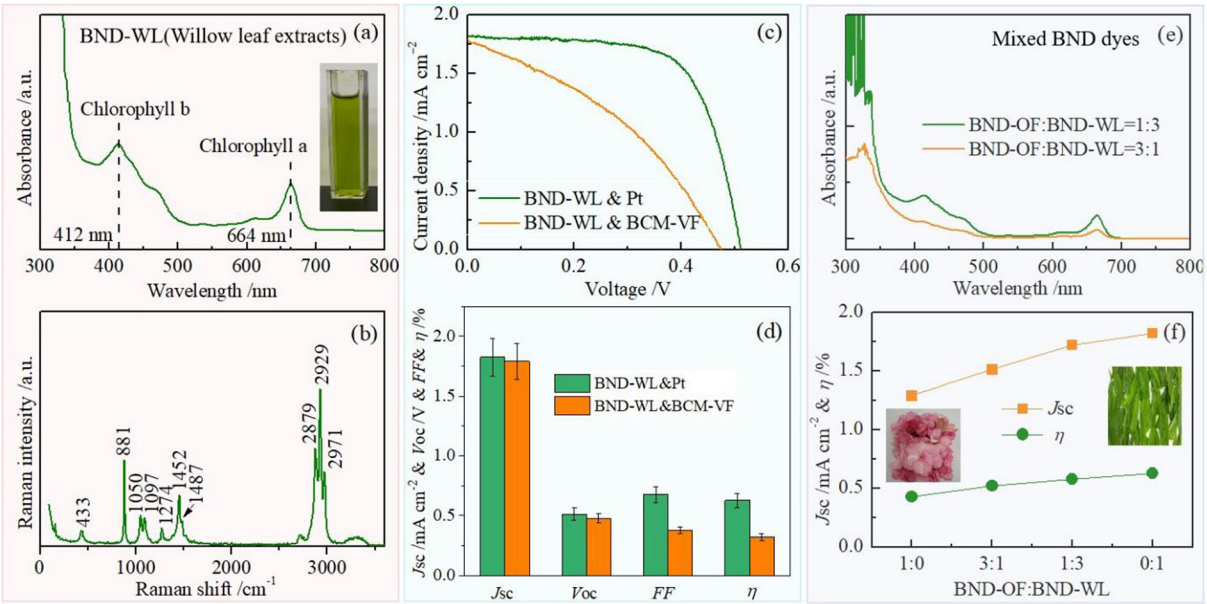

Fig. 8 (a) and (b) UV-Vis and FT-Raman spectra of BND-WL solution. (c) and (d) *J*–*V* curves and photovoltaic parameters of DSSCs using various dyes and counter electrodes. (e) UV-Vis spectra of the mixed solution of BND-OF and BND-WL, and (f) their photovoltaic parameters in DSSCs with a Pt electrode.

and a BCM-VF electrode, as shown in Fig. 8(c) and (d). Furthermore, BND-WL was also blended with BND-OF derived from the oleander flower to prepare a mixed BND. Unfortunately, the photovoltaic properties of the mixed BND used in the mono-biowaste-based DSSC with a Pt electrode were not further improved relative to those of BND-WL alone, mainly owing to the negligible complementarity of the absorption spectra of BND-WL and BND-OF, as demonstrated in Fig. 8(e), (f) and Fig. S5 (ESI†).

4. Conclusion

Renewable-flower-based DSSCs, including both mono-biowaste-based and dual-biowaste-based device modes, were assembled by applying BND dye or/and a BCM counter electrode. In the mono-biowaste-based devices with a Pt counter electrode, the BNDs extracted from five flowers were adopted as photosensitizers, and the devices exhibited η values varying from 0.17% to 0.43%. Anthocyanins, the main active components of BNDs, have subtly different structures, resulting in BNDs with varying light-capturing abilities. These differences in light-capturing abilities are a key factor contributing to the variation in photovoltaic performance among the cells. In other mono-biowaste-based devices with N719 dye, the BCM composed of amorphous carbon from the five pyrolyzed flowers are employed as the counter electrode catalysts. The η values of the five flower-based devices followed the sequence crape myrtle violet flower > crape myrtle white flower > lotus flower > oleander flower > hibiscus flower. The highest efficiency (2.13%) of the cell is mainly attributed to the unique microstructure and the *N*,*S*-codoped carbon skeleton with oxygen-containing groups of the BCM derived from the crape myrtle violet flower, which provide more catalytically active sites for electrolyte reduction. As the crape myrtle violet flower can provide a relatively pronounced dye and the most excellent electrode catalyst among the five flowers for the DSSCs, a dual-biowaste-based device with an η of 0.181% was fabricated by employing the corresponding BND photosensitizer and BCM electrode. Moreover, to improve the η of the above dual-biowaste-based device, a willow-leaf-extract BND with enhanced photon-capturing ability was further introduced to replace the crape myrtle violet flower extract BND, giving rise to an enhanced η of 0.32%.

Author contributions

Shunjian Xu: methodology, formal analysis, writing – original draft. Ping Huang: Formal analysis, writing – review & editing, funding acquisition. Wei Zhong: investigation, software. Yongping Luo: investigation, data curation. Haiyan Fu: methodology, data curation. Zonghu Xiao: resources, supervision. Hong Jin: validation, visualization. Yike Liu: writing – review & editing, project administration.

Data availability

Data will be made available upon considerable request.

Conflicts of interest

There are no conflicts of interest to declare.

Open Access Article. Published on 31 May 2025. Downloaded on 5/31/2026 5:17:34 AM. This article is licensed under a Creative Commons Attribution-NonCommercial 3.0 Unported Licence.

Acknowledgements

This research was financially supported by National Natural Science Foundation of China (52462008), Natural Science Foundation of Zhejiang Province (LY24E020007), Natural Science Foundation of Jiangxi Province (20232BAB204010), Guizhou Provincial Major Scientific and Technological Program (No. Qian Kehe Major Special Projects [2024]019) and Science and Technology Project of Huzhou (2023GZ59; 2024GZ16).

References

1 X. M. Cheng, K. T. Ye, A. M. Du, Z. Z. Bao and G. Chlomou, Dual carbon goals and renewable energy innovations, *Res. Int. Bus. Finance*, 2024, **70**, 102406.
2 M. Mirzaei and M. B. Gholivand, Ni and P co-doped WS2 nanosheets decorated on MWCNTs as an efficient counter electrode for dye-sensitized solar cells, *J. Alloy. Compd.*, 2024, **980**, 1.
3 R. Sasikumar, S. Thirumalaisamy, B. Kim and B. Hwang, Dye-sensitized solar cells: Insights and research divergence towards alternatives, *Renewable Sustainable Energy Rev.*, 2024, **199**, 114549.
4 D. Cao, A. Wang, X. Yu, H. Yin, J. Zhang, B. Mi and Z. Gao, Room-temperature preparation of TiO_2/graphene composite photoanodes for efficient dye-sensitized solar cells, *J. Colloid Interface Sci.*, 2021, **586**, 326.
5 W. Ding, C. Bai, Y. Ren, D. Fang, J. Bai, J. Wen, B. Mi, D. Cao and Z. Gao, Synergetic Effects of Recombination-blocking, Band-bending and Gap-state Manipulation by Interfacial Engineering in solid-state DSSCs comprising Cs_2SnI_6 electrolyte, *Surf. Interfaces*, 2024, **48**, 104246.
6 H. Z. Zhou, L. Q. Wu and Y. R. Gao, Dye-sensitized solar cells using 20 natural dyes as sensitizers, *J. Photochem. Photobiol., A*, 2011, **219**, 188.
7 G. R. Li and X. P. Gao, Low-cost counter-electrode materials for dye-sensitized and perovskite solar cells, *Adv. Mater.*, 2020, **32**, 1806478.
8 A. K. Mondal, K. Kretschmer, Y. F. Zhao, H. Liu, C. Y. Wang, B. Sun and G. X. Wang, Nitrogen doped porous carbon nanosheets from eco-friendly eucalyptus leaves as high performance electrode materials for supercapacitors and lithium ion batterie, *Chem. – Eur. J.*, 2017, **23**, 3683.
9 R. Syafinar, N. Gomesh, M. Irwanto, M. Fareq and Y. M. Irwan, Chlorophyll pigments as nature based dye for dye-sensitized solar Cell (DSSC), *Energy Proc.*, 2015, **79**, 896.
10 N. Mariotti, M. Bonomo, L. Fagiolari, N. Barbero, C. Gerbaldi, F. Bella and C. Barolo, Recent advances in eco-friendly and cost-effective materials towards sustainable dye-sensitized solar cells, *Green Chem.*, 2020, **22**, 7168.
11 S. Verma and G. Gupta, Natural dyes and its applications: A brief review, *Int. J. Res. Anal. Rev.*, 2017, **4**, 57.
12 M. Guan, X. J. Kang, L. Wei, X. J. Hu, C. Han, X. Li, H. W. Liu, L. Qu and Z. W. Zhao, A dual-mode strategy combining SERS with MALDI FTICR MS based on core-shell silver nanoparticles for dye identification and semi-quantification in unearthed silks from Tang Dynasty, *Talanta*, 2022, **241**, 123277.
13 G. Richhariya, A. Kumar, P. Tekasakul and B. Gupta, Natural dyes for dye sensitized solar cell: A review, *Renewable Sustainable Energy Rev.*, 2017, **69**, 705.
14 S. Narendhiran, S. Midya, P. L. Mahapatra, M. Balachandran, C. S. Tiwary, A. K. Singh and P. Kumbhakar, Nickel telluride quantum dots as a counter electrode for an efficient dye-sensitized solar cell, *ACS Appl. Electron. Mater*, 2024, **6**, 487.
15 G. Syrrokostas, A. Siokou, G. Leftheriotis and P. Yianoulis, Degradation mechanisms of Pt counter electrodes for dye sensitized solar cells, *Sol. Energy Mater. Sol. C*, 2012, **103**, 119.
16 L. Li and G. Li, Great enhancement in power conversion efficiency of DSSCs with Ni0.85Se nanoparticles as counter electrode in contrast to matrix nickel particles, *Funct. Mater. Lett.*, 2023, **16**, 11.
17 S. J. Xu, P. Huang, W. Zhong, Y. P. Luo, Z. M. Yan, L. Liu and Z. H. Xiao, Dual-biowaste-based dye-sensitized solar cells using natural chlorophyll dye and natural counter electrode derived from fallen leaves, *Appl. Phys. A: Mater. Sci. Process.*, 2023, **129**, 673.
18 S. J. Xu, C. Liu and J. Wiezorek, 20 renewable biowastes derived carbon materials as green counter electrodes for dye-sensitized solar cells, *Mater. Chem. Phys.*, 2018, **204**, 294.
19 N. Shahzad, L. Tahira Perveen, D. Pugliese, S. Haq, N. Fatima, S. M. Salman, A. Tagliaferro and M. I. Shahzad, Counter electrode materials based on carbon nanotubes for dye-sensitized solar cells, *Renewable Sustainable Energy Rev.*, 2022, **159**, 112196.
20 M. Gomathi, A. Sankar, S. Kannan, M. Shkir and V. R. M. Reddy, Tin selenide/carbon black nanocomposite-based high efficiency counter electrode for dye-sensitized solar cells (DSSCs), *Chem. Phys. Lett.*, 2022, **802**, 139802.
21 H. Choi, H. Kim, S. Hwang, W. Choi and M. Jeon, Dye-sensitized solar cells using graphene-based carbon nano composite as counter electrode, *Sol. Energy Mater Sol. C*, 2011, **95**, 323.
22 A. Jain, R. Balasubramanian and M. P. Srinivasan, Hydrothermal conversion of biomass waste to activated carbon with high porosity, *Chem. Eng. J.*, 2016, **283**, 789.
23 J. M. Dias, M. C. M. Alvim-Ferraz, M. F. Almeida, J. Rivera-Utrilla and M. Sánchez-Polo, Waste materials for activated carbon preparation and its use in aqueous-phase treatment, *J. Environ. Manage.*, 2007, **85**, 833.
24 S. Abbaszadeh, S. R. W. Alwi, C. Webb, N. Ghasemi and I. I. Muhamad, Treatment of lead-contaminated water using activated carbon adsorbent from locally available papaya peel biowaste, *J. Clean Prod.*, 2016, **118**, 210.
25 L. P. Xie, W. G. Lin and X. M. Yang, Factors affecting the adsorbability of activated carbons produced from municipal solid organic waste, *New Carbon Mater.*, 2006, **21**, 156.
26 J. H. Jiang, L. Zhang, X. Y. Wang, N. Holm, K. Rajagopalan, F. L. Chen and S. G. Ma, Highly ordered macroporous woody biochar with ultra-high carbon content as supercapacitor electrodes, *Electrochim. Acta*, 2013, **113**, 481.

© 2025 The Author(s). Published by the Royal Society of Chemistry

Open Access Article. Published on 31 May 2025. Downloaded on 5/31/2026 5:17:34 AM.
This article is licensed under a Creative Commons Attribution-NonCommercial 3.0 Unported Licence.

27 D. P. Qiu, C. H. Kang, M. Li, J. Y. Wei, Z. W. Hou, F. Wang and R. Yang, Biomass-derived mesopore-dominant hierarchical porous carbon enabling ultra-efficient lithium ion storage, *Carbon*, 2020, **162**, 595.
28 M. F. Hu, L. P. Huang, H. Li, G. J. Zhang and H. Z. Wu, Research progress on hard carbon anode for Li/Na-ion batteries, *J. Inorg. Mater.*, 2024, **39**, 32.
29 Q. W. Jiang, G. R. Li, F. Wang and X. P. Gao, Highly ordered mesoporous carbon arrays from natural wood materials as counter electrode for dye-sensitized solar cells, *Electrochem. Commun.*, 2010, **12**, 924.
30 W. Maiaugree, S. Lowpa, M. Towannang, P. Rutphonsan, A. Tangtrakarn, S. Pimanpang, P. Maiaugree, N. Ratchapolthavisin, W. Sang-aroon, W. Jarernboon and V. Amornkitbamrung, A dye sensitized solar cell using natural counter electrode and natural dye derived from mangosteen peel waste, *Sci. Rep.*, 2015, **5**, 15230.
31 V. A. Pereira Jr., I. N. Queiroz de Arruda and R. Stefani, Active chitosan/PVA films with anthocyanins from brassica oleraceae (red cabbage) as time-temperature indicators for application in intelligent food packaging, *Food Hydrocolloid*, 2015, **43**, 180.
32 S. S. Sahoo, S. Salunke-Gawali, V. S. Kadam and H. M. Pathan, Canna lily red and yellow flower extracts: A new power source to produce photovoltage through dye-sensitized solar cells, *Energy Fuel*, 2020, **34**, 9674.
33 Z. Jie, L. S. Wang, J. M. Gao, Q. Y. Shu, C. H. Li, J. Yao, Q. Hao and J. J. Zhang, Determination of anthocyanins and exploration of relationship between their composition and petal coloration in crape myrtle (Lagerstroemia hybrid), *J. Integr. Plant Biol.*, 2008, **50**, 581.
34 A. Braun, M. Bärtsch, B. Schnyder, R. Kötz, O. Haas, H. G. Haubold and G. Goerigk, X-ray scattering and adsorption studies of thermally oxidized glassy carbon, *J. Non-Cryst. Solids*, 1999, **260**, 1.
35 S. J. Xu, Y. F. Luo and W. Zhong, Investigation of catalytic activity of glassy carbon with controlled crystallinity for counter electrode in dye-sensitized solar cells, *Sol. Energy*, 2011, **85**, 2826.
36 W. Gu, D. W. Bousfield and C. P. Tripp, Formation of calcium carbonate particles by direct contact of $Ca(OH)_2$ powders with supercritical CO_2, *J. Mater. Chem.*, 2006, **16**, 3312.
37 S. Betancourt, L. J. Cruz and A. Toro, Effect of the addition of carbonaceous fibers on the tribological behavior of a phenolic resin sliding against cast iron, *Wear*, 2011, **272**, 43.
38 W. Yang, X. L. Ma, X. W. Xu, S. I. Raj, G. Q. Ning, A. J. Wang and S. L. Chen, Sulfur-doped porous carbon as metal-free counter electrode for high-efficiency dye-sensitized solar cells, *J. Power Sources*, 2015, **282**, 228.
39 C. K. Kim, I. T. Choi, S. H. Kang and H. K. Kim, Anchovy-derived nitrogen and sulfur co-doped porous carbon materials for high-performance supercapacitors and dye-sensitized solar cells, *RSC Adv.*, 2017, **7**, 35565.
40 E. C. Hao, W. Liu, S. Liu, Y. Zhang, H. L. Wang, S. G. Chen, F. L. Cheng, S. P. Zhao and H. Z. Yang, Rich sulfur doping porous carbon materials derived from ginkgo leaves for multiple electrochemical energy storage, *J. Mater. Chem. A*, 2017, **5**, 2204.